Eur. Phys. J. D **41**, 247–260 (2007)
DOI: 10.1140/epjd/e2006-00210-4

THE EUROPEAN PHYSICAL JOURNAL D

Homogeneous nucleation and growth in iron-platinum vapour investigated by molecular dynamics simulation

N. Lümmen and T. Kraska[a]

Physical Chemistry, University of Cologne, Luxemburger Str. 116, 50939 Köln, Germany

Received 2 June 2006 / Received in final form 17 August 2006
Published online 15 September 2006

Abstract. Homogeneous nucleation and growth from binary metal vapour is investigated by molecular dynamics simulation. It is focused here mainly on the iron-platinum system with a mole fraction of 0.5. The simulations are started in the highly supersaturated vapour phase. Argon is added as carrier gas removing the heat of condensation from the forming clusters. The embedded atom method is employed for modelling of the force field of iron and platinum. The simulation runs are evaluated with respect to the nucleation rate, monomer temperature, monomer amount, and with respect to the size of the largest cluster in the system including possible pure metal clusters. It turns out that depending on the composition of the complete system pure platinum clusters with sizes up to 10 to 15 atoms are formed in addition to binary clusters. Due to the high temperature of these clusters iron atoms less likely condense at the beginning of the particle formation simulation. This leads to temporary difference in the temperatures of the platinum and the iron subsystems, which eventually approach each other when only binary clusters are present. In summary, the results obtained from the cluster statistics show that pure platinum nucleation and growth can take place to some extent within the binary system.

PACS. 36.40.-c Atomic and molecular clusters – 71.15.Pd Molecular dynamics calculations (Car-Parrinello) and other numerical simulations – 81.10.Aj Theory and models of crystal growth; physics of crystal growth, crystal morphology, and orientation – 64.70.Nd Structural transitions in nanoscale materials

1 Introduction

1.1 Nucleation in pure and binary systems

Homogeneous nucleation is the first step in the formation of a new phase. In case of a condensation process the formation of a cluster of a new liquid phase is caused by density fluctuations of the supersaturated vapour phase. If such first cluster becomes large enough to pass an activation barrier it likely continues to grow to a stable droplet or particle. This activation barrier for the nucleation process is characterised by the so-called critical nucleus size and the critical work of formation. With increasing supersaturation the height of this activation barrier decreases and the nucleation rate, being the number of clusters per volume and time, which continue to grow, rises. Within classical nucleation theory [1,2] the activation barrier is a result of the balance between the different contributions to the free enthalpy of the system. These are the bulk properties of the newly formed cluster, droplet, or particle and its surface energy. While the classical nucleation theory still serves as a simple and useful model for the description and analysis of nucleation processes, in recent decades several further developments [3,4] and entirely new approaches [5–8] have been proposed.

The experimental data for homogeneous nucleation in part agree reasonably well with the classical nucleation theory [9,10]. For some systems corrections to the classical nucleation theory are necessary in order to get agreement with experimental data [11]. There are also systems for which the classical nucleation theory fails. Argon, although having rather simple van der Waals interactions, is a case for such large deviation to the classical nucleation theory [12].

It is also focused on the homogeneous nucleation in binary systems in experimental as well as theoretical investigations. Classical nucleation theory can be extended to binary systems in principal; however, several special features have to be taken into account. Depending on the specific binary system it can happen that the distribution of the different species is not homogeneous in the cluster. One species can be enriched at the surface for example [13–15], which of course affects the surface tension of the cluster. For example, it has been found recently that water/n-butanol nanodroplets consist of a mainly aqueous core with n-butanol enrichment at the surface [16]. The kinetic pre-factor of nucleation models has also been extended to binary systems [17,18]. Furthermore,

[a] e-mail: t.kraska@uni-koeln.de

a parameter describing the state of the system prior to nucleation has to be determined for binary nucleation. For pure substances this is the supersaturation defined as the ratio of vapour pressure of the system and the vapour pressure of the nucleating substance at the same temperature. For binary mixtures instead of the supersaturation the activity of each species is often used as order parameter [19,20]. The activity is the partial pressure of one species divided by the pure substance vapour pressure at the same temperature while the supersaturation in binary systems is the ratio with respect to the partial pressure over a mixture with the same mole fraction. Also, the nucleation theorem developed for pure substances [21–23] leading to a fundamental relation between the slopes of the nucleation isotherms and the number of atoms in the critical nucleus can be extended to binary systems [19]. While several experimental investigations on binary nucleation of molecular fluids have been published [19,24–28] there is little available on binary nucleation of metals. There are some experimental investigations of the nucleation in pure metal vapour providing data for the nucleation rate [29–31] but not yet for binary metal systems.

The nucleation process in binary systems in general is an important step in the complete particle formation process. With increasing nucleation rates, for example, the number of particles increases while the size of the particles decreases due to the faster decay of the supersaturation. The nucleation rate can also indirectly affect the particle morphology. A low nucleation rate leads to few particles that grow by surface growth rather than by coalescence or agglomeration. For a high nucleation rate many particles are present leading to higher collision probability and hence rather to agglomerated particles at given conditions. In case of two-component nucleation there are several other properties of interest. Especially in case of strongly attractive atomic systems such as metals the condensation heat leads to a strong heating up of the clusters. Here it is of interest how two systems with different attraction forces interact in this respect.

1.2 The FePt system

The FePt system is of interest in different technological areas. This includes its function as catalyst [32] as well as its potential as high-density data storage medium [33]. In the latter case it is focused on the production of 4 nm size nanoparticles with an ordered face centred tetragonal structure namely the $L1_0$ structure. In structural studies of FePt nanoparticles using X-ray diffraction the effect of composition on the tetragonality of the $L1_0$ structure has been investigated [34]. It has been found that the tetragonal distortion expressed by the c/a lattice constant ratio is at its maximum at a composition of 0.5. In that work is has also been shown that the corresponding minimum of the c/a lattice constant ratio at 0.966 is related to a maximum in the coercivity being the hysteresis of the magnetisation process. The coercivity is related to the lifetime of a magnetised state and hence to the period of time data can be stored. There are two major processes for the formation of FePt nanoparticles. In the liquid phase process [35] precursor substances such as metal carbonyls are heated in organic solvents until the precursor substances decompose and the metal atoms start to form particles. The vapour phase preparation method [36] is based on the formation of highly supersaturated metal vapours by, for example, sputtering which leads to particles in the gas phase by nucleation, growth, and agglomeration or coalescence. The liquid phase method yields FePt particles with a disordered fcc structure. In order to obtain the desired ordered tetragonal $L1_0$ structure for a mole fraction of 0.5 one has to sinter the nanoparticles after they have been deposited on a support layer. However, this can lead to the coalescence of the supported particles resulting in larger particles [37]. In case of the vapor phase process nucleation and growth takes place in a stream of a carrier gas. This includes the sintering step leading to the $L1_0$ structure of the nanoparticles before they are deposited. In this way the particles are not affected once they are deposited which avoids the coalescence towards larger domains.

The focus of this work is on the investigation of the first step of the FePt particle formation in vapour phase processes. Besides the determination of kinetic parameters the effects of interaction, difference in interaction, and the composition of the formed clusters on the nucleation and growth process are investigated.

2 Method

2.1 Simulation method

We employ the molecular dynamics (MD) simulation technique in which the equations of motion of each atom in the force field of all other atoms are solved numerically by the velocity-Verlet-algorithm. The numerical increment of such simulations, the time step, is 1 fs. In all simulations periodic boundary conditions were used along with the minimum image convention. In order to mimic the experimental situation as close as possible we add Lennard-Jones-argon as carrier gas. The argon atoms interact via the same interaction potential with the iron and platinum atoms. As initial configuration 432 metal atoms of each sort are placed on a fcc lattice with the interatomic distances as large as possible within the given box dimension, in any case larger than the interaction range. In case of the $Fe_{0.2}Pt_{0.8}$ systems 275 iron atoms and 1097 platinum atoms were placed on the same lattice type. Earlier [38] we have already investigated the effect of different choices of the initial configuration on the course of the simulation and found no influence provided a large enough interatomic distance in the start configuration. In addition the two atomic sorts are here randomly distributed across the sites of the initial fcc lattice. After starting the simulation the time before the onset of nucleation and growth is large enough for further distribution of the metal atoms by diffusion, which makes the simulation independent of the initial configuration. A cluster is detected by the Stillinger criterion [39] with a cut-off distance of 0.35 nm. The maximum range of the employed potential model is 0.53 nm

for Pt and 0.4409 nm for Fe that is somewhat larger than the chosen Stillinger cut-off distance. This choice of the Stillinger cut-off avoids to a large extent to count events, where atoms/clusters pass by each in a distance so large that they unlikely will stay together in one cluster. We prefer this simple cluster detection criterion to other approaches [40–43] as the approximation for our purposes although it may slightly overestimate the cluster size. As done before for pure metal nucleation and growth [44,45] we have checked the influence of the choice of the Stillinger cut-off distance on the results and found no significant influence ±10% around the used value. The ratio between the sum of all metal atoms and argon is always Ar:Me 3:1. This corresponds to the value used for the nucleation rate determination in the pure Fe and pure Pt simulations [44,45]. The condensation heat is removed from the nucleating substances by collisions with the argon atoms only. The argon atoms themselves are coupled to a numerical MD thermostat that is implemented as simple velocity scaling. The use of other MD thermostats for the carrier gas has no influence on the results [46]. By using this method the nucleating substance is not influenced by a MD thermostat directly being very important for strongly attracting systems such as metals. The argon atoms themselves are placed randomly in the simulation box after the lattice with the metal atoms has been set up. In the initial configuration a minimum distance of $2.5\sigma_{\mathrm{Ar}}$ is kept between the argon atoms and all other atoms.

2.2 Potential model

In order to treat systems with several hundred up to few thousand atoms over a long simulation time we used the embedded atom method (EAM) [47–49] for modelling the force field acting between the atoms. This commonly used force field for metals contains two terms: the pairwise additive interaction ϕ of the atomic cores shielded at short interatomic distances is modelled by a screened Coulomb potential with effective charges $Z(r)$. For binary alloys of compounds A and B, this screened Coulomb potential reads

$$\phi_{ij} = \frac{Z_{A,i}(r_{ij}) Z_{B,j}(r_{ij})}{r_{ij}}. \tag{1}$$

Secondly the multi-body contribution $F[\rho]$, the embedding function, to the energy is modelled by a multi-body term assuming a linear superposition ρ of atomic electron densities ρ^{at}

$$\rho_i = \sum_{j=1, j\neq i}^{N} \rho^{\mathrm{at}}_{(j)}(r_{ij}) \tag{2}$$

which reflects the delocalisation of the neighbouring atoms' electrons. The index (j) selects the atomic electron density function of the sort atom j belongs to. The energy of an atom i can hence be written as

$$E_i = F_i\left[\rho_i\right] + \frac{1}{2}\sum_{i,j>i}^{N} \phi_{ij}(r_{ij}). \tag{3}$$

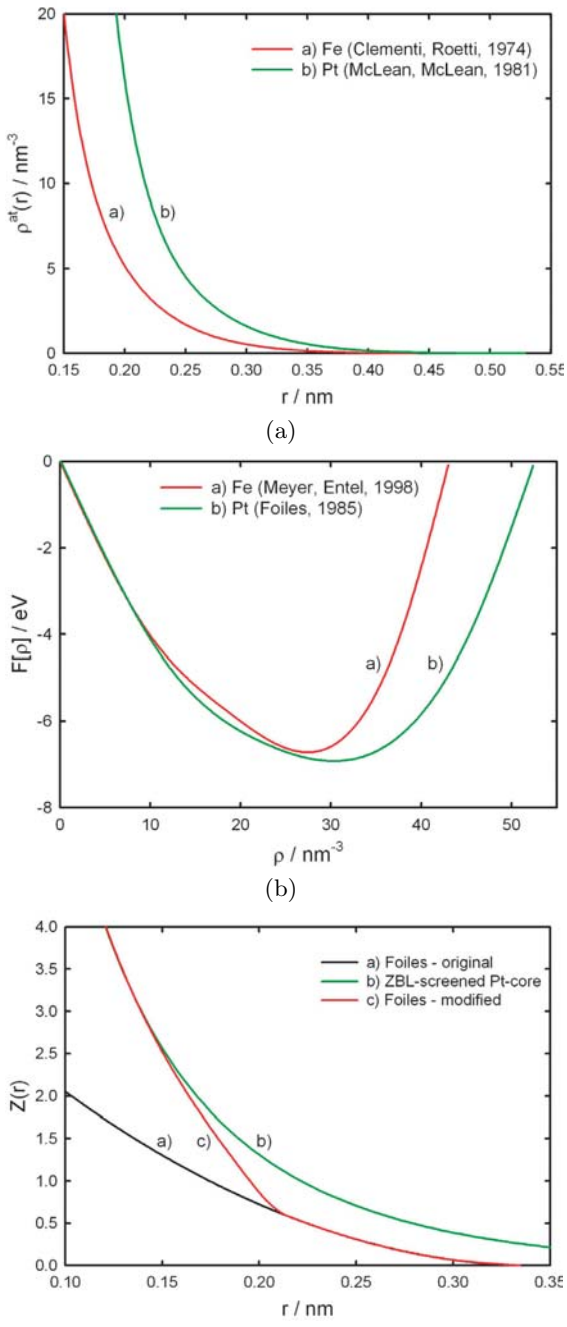

Fig. 1. (Color online) (a) Atomic electron densities $\rho^{\mathrm{at}}(r)$ (Eq. (4)) for an atom of Fe and Pt each; (b) embedding functions $F[\rho]$ for Fe and Pt where ρ is a superposition of atomic electron densities ρ^{at} (Eq. (3)); (c) effective charges $Z(r)$ for Fe and Pt.

The indices i and j run over the number of atoms N in the system.

The functions for the atomic electron density $\rho^{\mathrm{at}}(r)$, the embedding function $F[\rho]$, and the effective charge $Z(r)$ are all represented by natural cubic spline functions (Fig. 1). The atomic electron density functions are calculated from the valence electron Hartree-Fock double ζ

Table 1. Data for the screening function $Z(r)$.

r /nm	Z_{Fe}/e
0.0	26.0
0.2008	1.4403
0.2495	0.2452
0.2696	0.1491
0.3442	0.0

r /nm	Z_{Pt}/e
0.0	78.0
0.01	47.560
0.025	28.702
0.05	15.152
0.07	9.934
0.135	3.204
0.19	1.158
0.2145	0.587
0.215	0.583
0.235	0.417
0.25	0.311
0.3	0.066
0.33459	0.0

wave functions $\Psi(r)$ taken from the tables of Clementi and Roetti [50] and McLean and McLean [51]. They have a cut-off and are shifted to zero at a certain distance from the atom's core (iron: 0.4409 nm, platinum: 0.53 nm)

$$\rho^{\mathrm{at}}(r) = N_{\mathrm{s}} \left|\Psi_{\mathrm{s}}(r)\right|^2 + (N_{\mathrm{v}} - N_{\mathrm{s}}) \left|\Psi_{\mathrm{d}}(r)\right|^2 - \rho_{\mathrm{c}}. \quad (4)$$

Here, N_{v} is the number of valence electrons, N_{s} the effective number of s-electrons participating in the binding in the bulk phase and ρ_{c} the atomic electron density at the cut-off distance. This number is usually derived from the heat of solution of the material of interest.

For iron we used the EAM-potential published by Meyer and Entel [52] that we have already employed in various investigations on iron nanoparticle formation [38,53,54]. For the interaction between the platinum atoms we employ an EAM-potential by Foiles [55] with a modified effective charge $Z(r)$.

The spline knots for the effective charges are listed in Table 1. Those for iron are the original ones taken from the work of Meyer and Entel [52] with a cut-off-radius of $r_{\mathrm{c}} = 0.34418$ nm. Foiles used the following function for describing the effective charge of platinum [55]

$$Z_{\mathrm{Pt,Foiles}}(r) = \sqrt{a_1(r_{\mathrm{c}} - r)^3 + a_2(r_{\mathrm{c}} - r)^4} \quad (5)$$

with $a_1 = 0.065699$ and $a_2 = 0.110961$ and a cut-off radius of $r_{\mathrm{c}} = 0.33459$ nm. However, this function gives much too low value for small interatomic distances, which allows atoms to come unnaturally close in the vapour phase. For distances smaller than 0.2145 nm we use spline knots taken from a Ziegler-Biersack-Littmark-type (ZBL) screened Pt-core [56]. The knot at 0.19 nm in Table 1 is an average value from both curves. This modification makes the potential model more repulsive at these distances being necessary to prevent colliding atoms in the vapour phase to come too close. However, this modification does not affect the properties of the bulk phase for which the potential was originally constructed. The embedding functions $F[\rho]$ were used as tabulated in the works of Meyer and Entel [52] and Foiles [55] except the last point in Table III in [55] which was taken as $\rho = 0.052445$ Å^{-3} to be more repulsive at interatomic distances smaller than 0.215 nm.

2.3 Supersaturation and activities

In case of binary nucleation the activities of the two substances are usually employed in the analysis rather than the supersaturation. The activity is defined as the ratio of the pressure of substance i and the vapour pressure of pure substance i:

$$a_i = \frac{p_i(T)}{p_{\mathrm{vap},i}(T)}. \quad (6)$$

Choosing the activities describes the system as an ideal mixture. Although binary systems usually exhibit deviations to the real mixture the activities are used here for several reasons. First the activity is used in experimental investigations of binary nucleation and comparisons, quantitative but also qualitative ones, are possibly using the same coordinates. Secondly, activities are required for the application of the nucleation theorem in order to obtain the number of atoms in the critical nucleus [19]. And finally, the equilibrium phase behaviour including the vapour phase required for the calculation of the supersaturation is not available for the system investigated here. Employing molecular dynamics simulations or Gibbs-Ensemble Monte-Carlo simulations to determine the equilibrium phase behaviour would not lead to results within reasonable simulation time for the systems investigated here. The reason is the low vapour pressure of the metals, which would require an extremely large volume for the vapour phase in such calculations.

The vapour pressure of the metal is calculated from the number of metal atoms, the temperature and the box volume using the ideal gas law applied to each metal separately. The vapour pressure is obtained from correlations given in the literature [57]. There are two ways to calculate the activities: first one can calculate it from the initial conditions that are determined by the temperature of the carrier gas and the total number of metal atoms of each sort. Secondly one can use the actual temperature of the metal monomers of each sort in the system and their actual amount. The monomer temperature and the number of monomers has been averaged over the period of time in that nucleation and initial growth take place. For pure substance particle formation we have employed both methods and found a very systematic behaviour of the nucleation rates as function of supersaturation based on the actual number of metal monomers and the metal monomer temperature. The reason for the latter way of calculating the supersaturation is that one can to some extent eliminate the influence of the relatively low amount of carrier gas in the simulations compared to experimental investigations. The amount of carrier gas affects the temperature of the system including the metal monomer temperature. In general the less carrier gas there is the higher is the metal monomer temperature. In experiments there is usually much more carrier gas and the temperature of the system is dominated by the carrier gas which can be used as basis for the calculation of the supersaturation. Using low amounts of carrier gas in the simulations heats up the metal monomers so that they are at the time when nucleation takes place actually at a temperature higher than

that of the carrier gas. However, this elevated temperature is the basis temperature of the nucleation process. In addition we have also calculated the supersaturation based on the carrier gas temperature and the total amount of monomers of each atom sort in the start configuration.

2.4 Nucleation rates

For the calculation of the nucleation rate we employ a method of Yasuoka and Matsumoto [58] using the cluster statistics to locate the period of time in which the nucleation takes place. If there are enough clusters in the system one can plot the number of clusters larger than a threshold value against the simulation time and gets a linear ascent over a certain time interval. The slope of this linear domain divided by the simulation volume gives the nucleation rate. We have applied this method straightforward for the binary systems investigated here. For very low activation barriers nucleation and growth may take place leading to an effective nucleation rate. However in systems heating up strongly lower supersaturation can be achieved where nucleation is more likely.

3 Results

3.1 Growth curves

Particle growth can be represented in different ways. Here we use the average cluster size as well as the maximum cluster size as order parameters for the growth. In Figure 2a the average cluster size including the monomers is plotted for three independent simulations at the same conditions, the same carrier gas temperature, the same density, and the same composition. Up to four nanoseconds the three curves are virtually indistinguishable and very smooth. At about 4 ns the curves exhibit some kinks and continue slightly different. These kinks are related to cluster collisions leading to a significantly larger cluster in one step. Due to the averaging of the cluster size a cluster collision does not lead to strong change these grow curves. The size of the largest cluster in the simulation system is plotted in Figure 2b for three independent simulations for a carrier gas temperature of 1000 K. Here again all three curves are very close at the beginning of the simulation and deviate only later. In this region the curves are rather smooth which indicates nucleation and growth by condensation of vapour atoms at the largest cluster. After 1.5 ns the curve exhibits jumps in the cluster size that are related to cluster collisions. The plot of the largest cluster size emphasises collisions stronger than the plot of the average cluster size does. Both plots in Figure 2 show that the growth of independent runs is reproducible in the time period where nucleation and initial growth take place. The deviations later on are related to cluster collisions which are stochastic events leading to different developments of the simulation systems.

In the systems investigated here nucleation takes place mainly within the first four nanoseconds. Due to the slow exchange of heat between the clusters by collision with

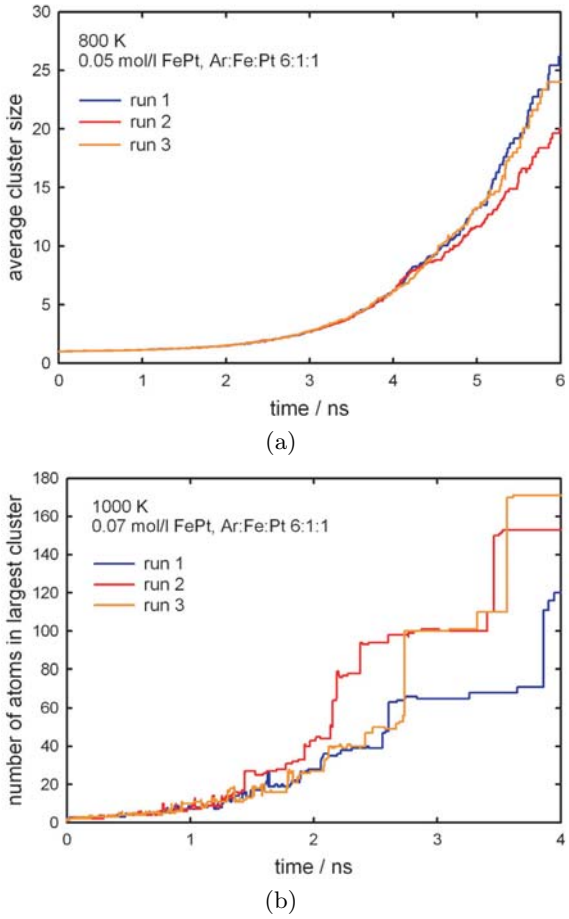

Fig. 2. (Color online) (a) Growth curves of three independent runs at a carrier gas temperature of 800 K based on the average cluster size. (b) Growth curves of three independent runs at a carrier gas temperature of 1000 K based on the largest cluster in the system.

the carrier gas atoms they behave quasi-adiabatic at the beginning of the nucleation and heat up [59]. In order to analyse the details of the binary nucleation process we have plotted the number and the temperature of the remaining Fe and Pt monomers separately. Figure 3a shows that the monomer temperature of both atom sorts is very similar during the first nanosecond. After one nanosecond the temperatures of the monomers of both atom sorts fluctuate stronger which is due to the increasingly bad statistics since the number of monomers decreases continuously. In addition the temperature of the Fe monomers is slightly above that of the Pt monomers. It is interesting to note that the average temperature of all Pt atoms in the system is above the average temperature of all Fe atoms, at least for the first three nanoseconds as shown in Figure 3b. Only thereafter the temperature of the Fe and the Pt subsystems approach the same value within the usual thermal fluctuations. The reason for this behaviour is the different growth rate of Pt and Fe as shown in Figure 3c by the number of monomers in the system. At the very beginning the number of Pt and Fe monomers is the same but then the number of Pt monomers decreases faster. The number

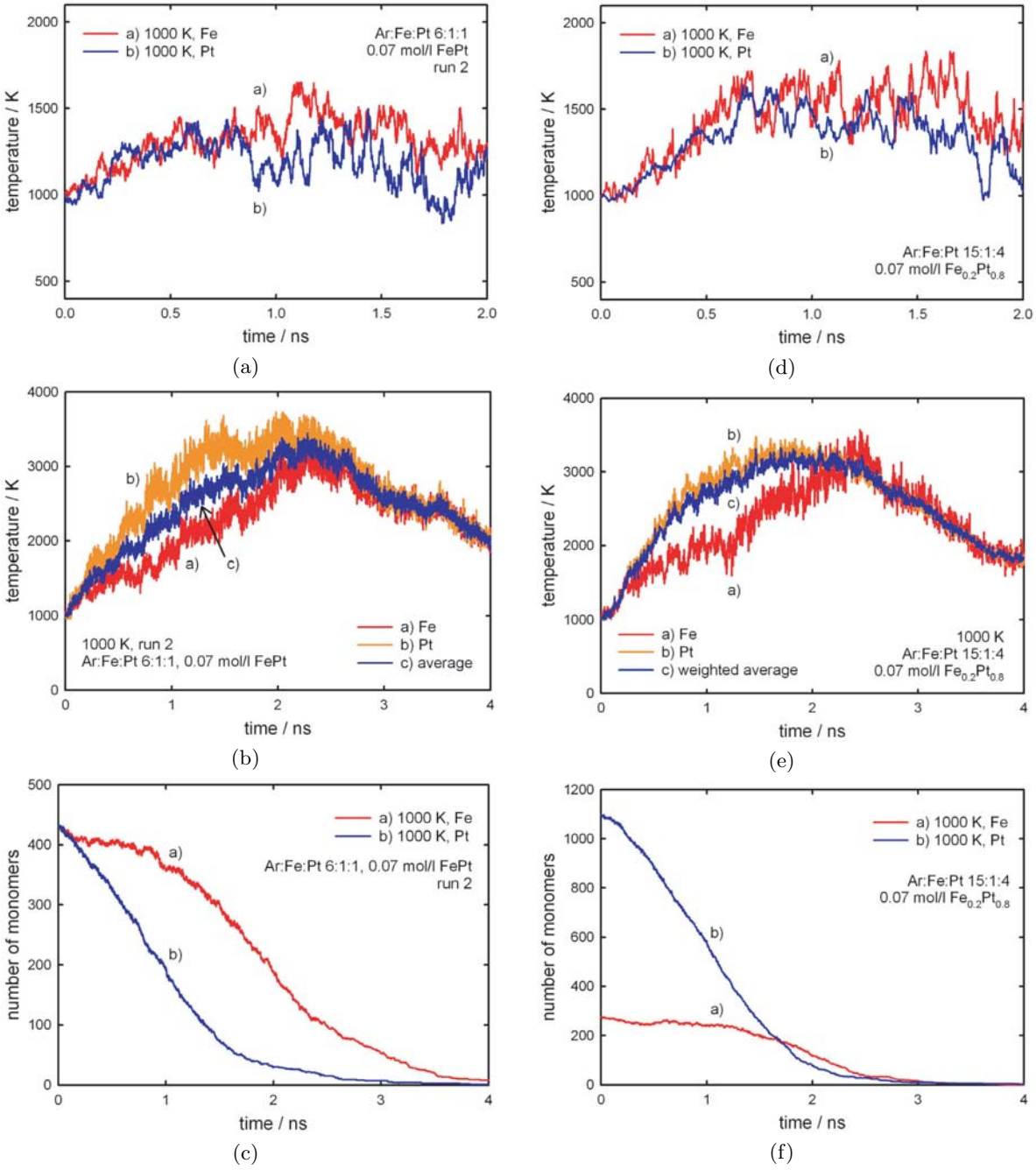

Fig. 3. (Color online) (a) Temperature of the metal monomers in the gas phase. (b) Temperature of all Fe atoms, all Pt atoms and the total system. (c) Number of Fe and Pt monomers in the system. (d) As (a) but with $x_{\mathrm{Pt}} = 0.8$. (e) As (b) but with $x_{\mathrm{Pt}} = 0.8$. (f) As (c) but with $x_{\mathrm{Pt}} = 0.8$.

of Fe monomers follows with a delay of approximately one nanosecond. As Pt grows apparently faster than Fe and since the clusters are only weakly thermally coupled via collisions with the carrier gas atoms, the average temperature of the Pt atoms can increase above that of the Fe atoms.

Simulations with a composition $x_{\mathrm{Pt}} = 0.8$ exhibit very similar behaviour as for $x_{\mathrm{Pt}} = 0.5$. The Pt and Fe monomer temperatures shown in Figure 3d increase to higher values than for $x_{\mathrm{Pt}} = 0.5$ (Fig. 3a). Also the temperature of the Fe monomers is higher than the Pt monomer temperature. The temperature of the Pt subsystem is closer to that of the complete system (Fig 3e) simply because there are more Pt atoms in the system. The difference to the Fe temperature is clearly visible. The number of Pt monomers decreases faster than the number of Fe monomers (Fig. 3f) as for $x_{\mathrm{Pt}} = 0.5$. Although there is 4 times more Pt as Fe in the system the number of Pt monomers can even become smaller than the number of Fe monomers due to the faster nucleation and growth of Pt.

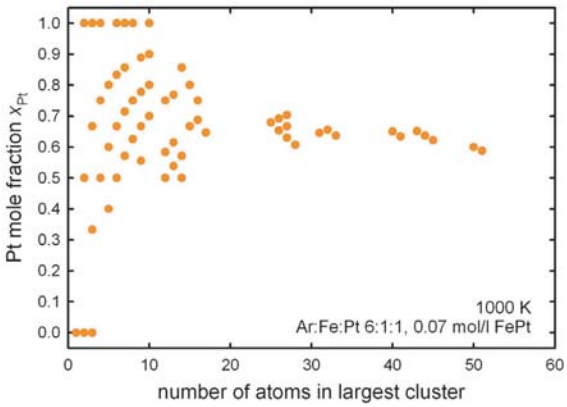

(a)

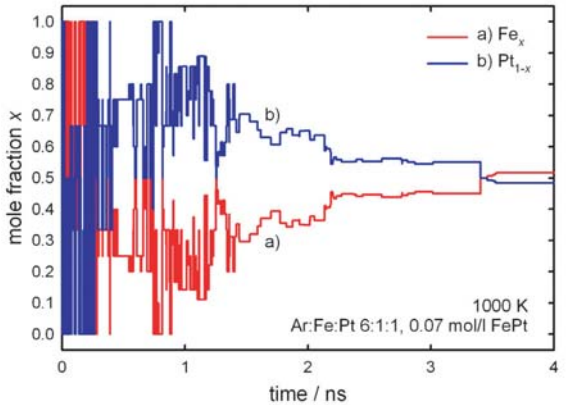

(b)

Fig. 4. (Color online) (a) Mole fraction of the largest cluster in the system. (b) Mole fraction of the largest cluster plotted against the size of the largest cluster.

For every available configuration, the size, composition, and temperature of the largest cluster have been determined. Figure 4a shows the mole fraction of Pt in the largest cluster plotted against the number of atoms in the largest cluster. The composition of the largest cluster fluctuates, especially at the beginning for small cluster sizes. One also finds that the largest cluster can consist of up to ten Pt atoms being a pure Pt cluster (see points at the top of Fig. 4a) while pure Fe clusters can be found only up to trimers (see points at the bottom of Fig. 4a). Such Pt_{10} cluster has a high temperature leading to an average Pt temperature above that of the Fe subsystem. Figure 4a also shows that thereafter the mole fraction of the largest cluster proceeds quickly towards a value of 0.5 being the initial vapour phase composition of the system. In Figure 4b the composition of the largest cluster is plotted against the simulation time. At the beginning there are huge fluctuations since the clusters consist of a few atoms only. After about 0.5 ns Pt atoms dominate the largest cluster with a Fe mole fraction roughly around 0.3. Due to the growth by condensation and by collisions with other clusters, for example at about 3.5 ns, the composition of the largest cluster approaches the value 0.5. This figure also shows that the amount of Pt at the beginning of the cluster formation process is higher than that of Fe.

4 Cluster statistics

The analysis of the largest cluster in the system gives already some hints that there are apparently clusters of pure Pt involved in the nucleation and growth process. For further investigation the cluster statistics is extracted from the simulations. First the number of all clusters of a certain size is averaged over one nanosecond simulation time and plotted in Figure 5a for a simulation with a carrier gas temperature of 1000 K. The error of this data depends on the time period used for the averaging because the cluster size distribution is continuously and systematically changing from the beginning of that time period until its end. Comparisons of the averaging over one and 0.5 ns shows that the error is in the order of few (2 to 3) clusters. In the first nanosecond the cluster size distribution is a monotonously decreasing function with a large amount of small clusters such as dimers and trimers. In the next nanosecond the cluster size distribution is still monotonously decreasing but shifted to larger cluster sizes simply because the clusters grow. However, in the time interval between three and four nanoseconds the size distribution exhibits a minimum at the trimer size. This is because at this point in time the supersaturation is reduced significantly leading to a lower effective nucleation rate and hence no new small clusters such as dimers are formed. From this time on the existing clusters continue to grow but no new clusters are formed. This point of time can therefore be regarded as the endpoint of nucleation in the specific simulation system. Hence the maximum of the cluster size distribution shifts to larger values. Due to the total system size there are only few larger clusters leading to a flat distribution. Another reason for the flatness is the averaging over one nanosecond. This averaging is necessary in order to obtain a smooth distribution based on a significant amount on configurations. Here 1000 configurations are averaged for one nanosecond.

The cluster size statistics of the mixed clusters only, e.g. those with both Fe and Pt atoms, is shown in Figure 5b. Since there are no mixed monomers the distribution function always has a maximum. Here one can observe more clearly the shift of the maximum towards larger cluster sizes with proceeding time. With the exception of the monomer and dimer amount the distribution functions look very similar to the distribution of all clusters (Fig. 5a). The difference between the distribution functions shown in Figures 5a and 5b is that the clusters consisting of one atom sort only are missing. The amount of pure Pt clusters is plotted in Figure 5c. It appears that there is a significant amount of pure Pt clusters present, even for trimers and tetramers. While in the first two nanoseconds the distribution function is monotonically decreasing it even exhibits a maximum in the third nanosecond. In analogy to the discussion above the appearance of this maximum can be discussed as the end of

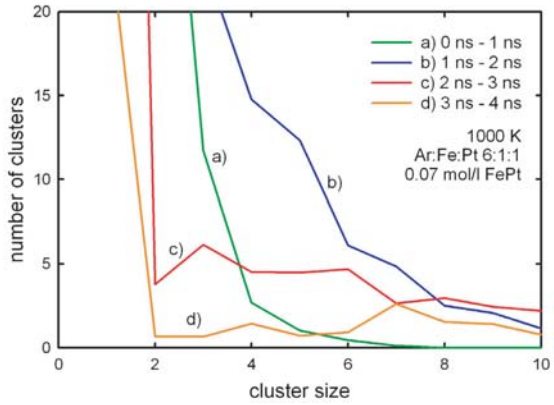

(a)

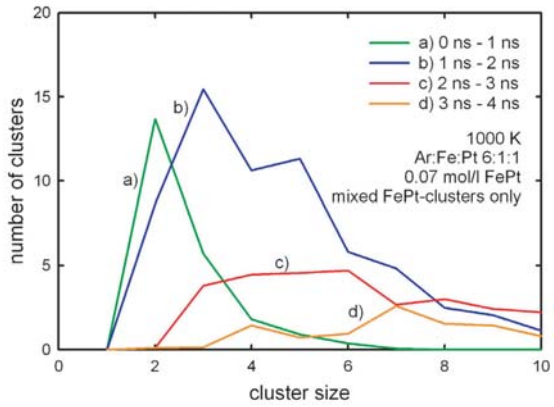

(b)

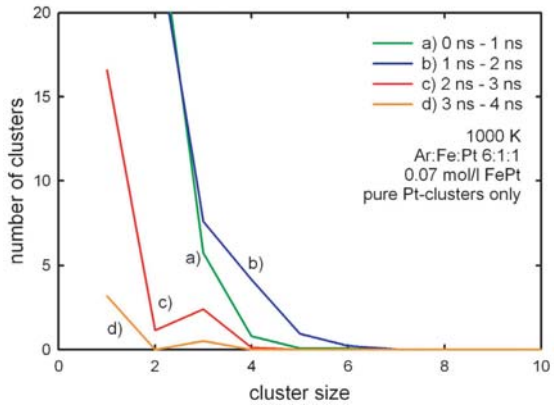

(c)

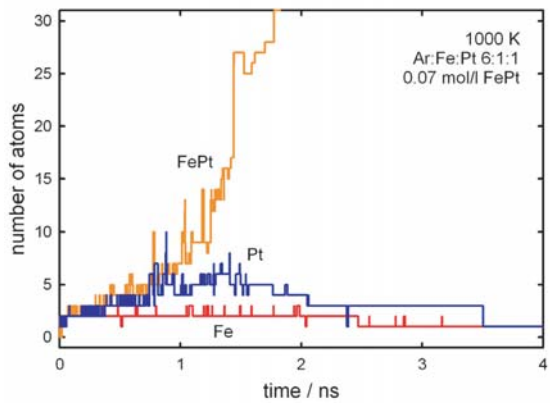

(d)

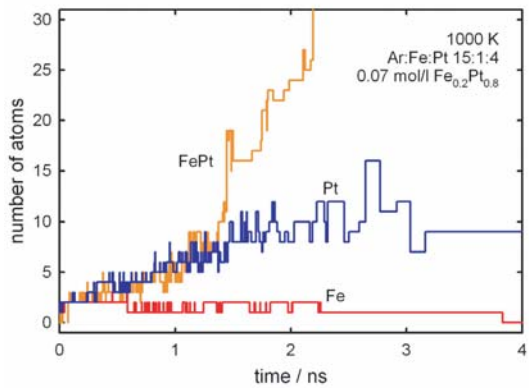

(e)

Fig. 5. (Color online) (a) Cluster size distribution averaged over a one nanosecond time interval. (b) Size distribution of the mixed clusters, excluding the clusters consisting of one atom sort only. (c) Size distribution of the clusters consisting of Pt atoms only. (d) Number of atoms in the largest clusters consisting of Pt atoms only, of Fe atoms only, and mixed clusters. (e) As (d) but for $x_{\mathrm{Pt}} = 0.8$.

significant nucleation in the simulation system. This is because a maximum can only appear if no new small clusters are formed by nucleation. It seems that the Pt subsystem actually undergoes a pure Pt nucleation, at least partially. The same plot for the Fe subsystem (not shown here) only shows very few dimers and even less trimers but clearly no pure Fe nucleation. The size of the largest mixed cluster, the largest pure Pt clusters, and the largest pure Fe clusters are plotted in Figure 5d. One can see that the largest mixed and the largest pure Pt cluster grow similar up to about 1.5 ns in this specific simulation. The size of the largest Fe cluster already deviates from the other two after less than 0.5 ns. After about 1.0 ns the size of the largest mixed cluster starts to deviate strongly from that of the largest pure Pt cluster. This is consistent with results discussed above indicating that pure Pt nucleation takes place and interferes with the nucleation of the binary system. This effect is larger in systems with higher Pt amount as shown in Figure 5e for $x_{\mathrm{Pt}} = 0.8$. Here the largest pure Pt cluster contains up to 16 atoms, which can be explained by the excess of Pt atoms in the system.

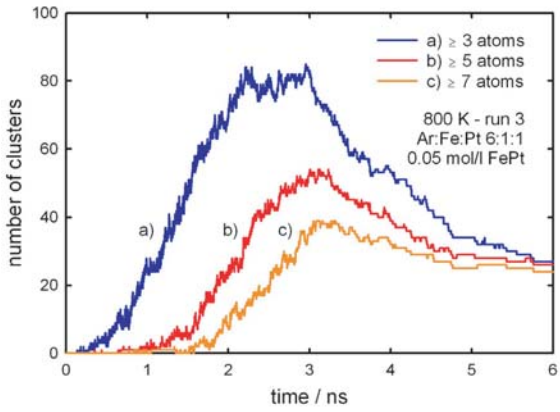

(a)

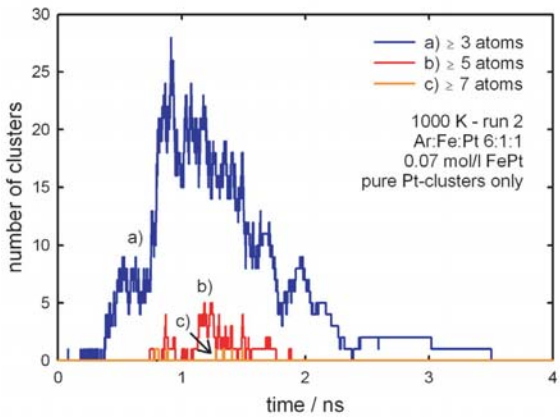

(b)

Fig. 6. (Color online) (a) Yasuoka-Matsumoto diagram for the determination of the nucleation rate using all clusters (pure and mixed). (b) Yasuoka-Matsumoto diagram for pure Pt clusters only.

4.1 Nucleation rates

The effective nucleation and growth rates are calculated from the cluster size statistics by the method of Yasuoka and Matsumoto [58] as described above. In Figure 6a an example for such analysis is shown. The number of clusters larger than a certain size threshold such as trimers, pentamers, and heptamers is plotted against the simulation time. One can see that for all size thresholds linear ascends are present. The nucleation rate is the slope of this linear domain divided by the volume of the simulation box. The different threshold values have only a small influence on the slope in the region where nucleation takes place. These plots have been evaluated for all simulations performed here at four different metal densities, three different carrier gas temperatures, and three independent runs for each state point. All obtained nucleation rates are listed in Table 2a together with the activities calculated from the number of the corresponding monomers and their temperature averaged over the time period of nucleation. The data are plotted together with the nucleation rates of the pure substances [44,45] in Figures 7a and 7b. The Pt nucleation rates are on the side with $\log(a_{\mathrm{Fe}}) = 0$ and vice versa. The binary nucleation rates for the composition $x_{\mathrm{Pt}} = 0.5$ are in the body of the diagram. Some data points for $x_{\mathrm{Pt}} = 0.8$ are added for comparison. The methodological error of the nucleation rates lies within the size of the symbols in Figure 7a and 7b. Therefore, error bars have been left out in the diagrams.

Figure 7b shows the same set of data as Figure 7a but it is a view onto the $(a_{\mathrm{Fe}} - a_{\mathrm{Pt}})$-plane to point out the following: As indicated by an arrow in Figures 7a and 7b the activity of the iron subsystem in the binary mixture is smaller as for a corresponding Fe system. This is related to a higher temperature of the Fe monomers in the binary system than in the pure Fe system. In case of Pt the effect is vice versa. The Pt monomers in the binary systems have a lower temperature (Tab. 2a) than the monomers in a corresponding pure Pt system and hence the activity in the binary system is higher. The reason for the temperature differences of the binary subsystems compared to the pure substance systems is related to the heat transfer between the two subsystems in the binary system. Due to its stronger interaction the Pt subsystem nucleates first. Condensed Fe atoms evaporate again because the Pt clusters can become very hot. Therefore, Fe in part acts here effectively as an additional carrier gas, which takes heat from the forming Pt clusters, at least at the beginning of the particle formation process. Hence, the Fe monomers have a higher temperature in the binary system than in the comparable pure Fe-system at the same state conditions, which originates from Pt nucleation in the binary system. This is clearly visible in Figures 7a and 7b. In an experimental study of homogeneous PdPt-nucleation by Rousset et al. [60] pure Pt-clusters up to a size of 10 atoms have been found in the mass spectrum. Furthermore, small clusters were richer in Pt than in Pd although the vapour phase consisted of 65% Pd. Like Fe, Pd has a lower cohesive energy compared to Pt and the authors suspected that small $\mathrm{Pd}_n\mathrm{Pt}_m$ clusters were supposed to cool by evaporation of Pd atoms. With our simulations we get a detailed insight into the particle formation process confirming the interpretation of the experimental results.

We have also looked into the possibility to correlate the binary nucleation data together with the pure Fe and Pt nucleation data using a function $\log J = f(\log a_1, \log a_2, T)$. Such correlation function can be constructed by extending the pure substance correlation functions $\log J = f(\log a_1, 0, T)$ and $\log J = f(0, \log a_2, T)$ [45,59] weighted by an activity fraction and with an additional binary cross-term including further adjustable parameters. This results in a circular or oval-like correlation function in the $\log(a_1)$ $\log(a_2)$ section for constant nucleation rate. One possible example for such correlation is shown in Figure 7g. This diagram also shows that the section of such three-dimensional function $\log J = f(\log a_1, \log a_2, T)$ at constant $\log a_1$ (here $\log a_{\mathrm{Pt}}$) exhibits a minimum in $f(\log a_2)$ and vice versa. Since the derivative in such section at constant $\log a_j$ is related to the number of atoms of sort $i \neq j$ in the critical nucleus by the binary nucleation theorem $(\partial \ln J / \partial \ln a_i)_T = N_i^* + 1$ [19], one obtains a negative number of atoms in the

Table 2. (a) Nucleation rate date for the binary FePt systems. The activities are calculated from the number of monomers and the monomer temperature averaged over the time period of nucleation. (b) Nucleation rate date for the binary FePt systems. The activities are calculated from the carrier gas temperature and the number of metal atoms is the vapour phase prior to nucleation being the total number of metal atoms of each species. The nucleation rates obtained from three independent simulations are averaged. (c) As (b) but for pure Fe. (d) As (b) but for pure Pt.

(a)

T(Ar)/K	ρ(Me)/mol dm^{-3}	T_{mon}(Me)/K	T_{mon}(Fe)/K	T_{mon}(Pt)/K	log(a_{Fe})	log(a_{Pt})	log(J/m^{-3}s^{-1})
800	0.07	1145.7	1177.3	1033.9	12.31	24.88	33.32
	0.07	1173.0	1208.5	1031.8	12.88	24.88	33.45
	0.07	1140.9	1175.8	1022.8	13.24	25.50	33.37
	0.05	1088.8	1107.3	1045.9	13.60	22.55	32.93
	0.05	1133.2	1168.6	1040.0	12.08	23.21	33.06
	0.05	1115.2	1131.5	1080.6	11.96	22.61	33.03
	0.035	1098.7	1151.4	1037.5	11.71	22.33	32.67
	0.035	1103.6	1113.2	1009.2	13.51	25.98	32.66
	0.035	1124.8	1131.5	1080.6	12.75	22.18	32.79
	0.02	1062.5	1094.5	996.83	12.84	22.86	32.04
	0.02	1046.5	1075.3	982.26	13.08	23.20	32.06
	0.02	1066.2	1081.8	1034.8	13.55	23.72	32.14
900	0.07	1251.9	1291.2	1143.1	10.45	21.30	33.36
	0.07	1229.7	1254.4	1157.1	10.68	22.88	33.34
	0.07	1322.0	1338.2	1280.0	10.67	18.84	33.36
	0.05	1218.4	1252.3	1099.4	10.45	24.34	33.10
	0.05	1276.7	1316.6	1167.0	10.04	22.48	33.10
	0.05	1235.0	1260.4	1174.9	10.08	19.92	32.94
	0.035	1197.5	1233.1	1072.7	10.78	23.61	32.67
	0.035	1183.6	1240.5	1098.9	10.33	21.11	32.66
	0.035	1183.6	1238.2	1037.9	11.33	25.45	32.71
	0.02	1184.2	1224.5	1093.2	10.29	19.71	32.21
	0.02	1199.7	1222.7	1140.2	10.38	19.51	32.17
	0.02	1155.2	1182.2	1033.8	11.16	20.92	32.09
1000	0.07	1363.2	1384.5	1291.2	8.91	20.17	33.31
	0.07	1351.7	1411.0	1184.3	9.42	20.59	33.42
	0.07	1346.1	1399.1	1205.8	9.83	20.54	33.41
	0.05	1342.5	1369.6	1256.3	8.95	19.88	33.09
	0.05	1312.1	1342.9	1201.8	9.40	25.09	32.98
	0.05	1343.9	1383.8	1221.1	9.01	20.47	32.99
	0.035	1305.9	1331.9	1231.1	9.46	18.56	32.67
	0.035	1285.8	1316.3	1111.0	10.08	22.52	32.61
	0.035	1260.5	1291.2	1191.9	9.97	20.68	32.63
	0.02	1244.6	1280.7	1147.2	10.32	24.56	32.04
	0.02	1241.6	1265.6	1161.2	10.04	23.11	32.03
	0.02	1285.5	1300.3	1224.6	9.55	19.04	32.26

(b)

T(Ar)/K	x_{Pt}	ρ(Me)/mol dm^{-3}	log(a_{Fe})	log(a_{Pt})	log(J/m^{-3}s^{-1})
800	0.5	0.07	18.48	27.54	33.39
800	0.5	0.05	18.33	27.40	33.01
800	0.5	0.035	18.18	27.24	32.71
800	0.5	0.02	17.94	27.00	32.08
900	0.5	0.07	15.81	23.87	33.35
900	0.5	0.05	15.67	23.72	33.05
900	0.5	0.035	15.51	23.56	32.68
900	0.5	0.02	15.27	23.32	32.15
1000	0.5	0.07	13.68	20.93	33.38
1000	0.5	0.05	13.54	20.78	33.02
1000	0.5	0.035	13.38	20.63	32.64
1000	0.5	0.02	13.14	20.38	32.11
800	0.8	0.07	18.08	27.75	33.48
900	0.8	0.07	15.42	24.07	33.38
1000	0.8	0.07	13.29	21.13	33.42

Table 2. *Continued.*

(c)

T(Ar)/K	ρ(Fe)/mol dm^{-3}	T_{mon}(Fe)/K	$\log(a_{\mathrm{Fe}})$	$\log(J/\mathrm{m}^{-3}\mathrm{s}^{-1})$
800	0.07	852	18.79	33.34
800	0.05	836	18.64	33.39
800	0.035	842	18.48	32.65
800	0.02	836	18.26	32.13
900	0.07	949	16.12	33.51
900	0.05	937	15.97	32.92
900	0.035	920	15.82	32.64
900	0.02	935	15.59	32.06
1000	0.07	1041	13.99	33.33
1000	0.05	920	13.84	33.01
1000	0.035	1030	13.69	32.67
1000	0.02	1000	13.46	32.10

(d)

T(Ar)/K	ρ(Pt)/mol dm^{-3}	T_{mon}(Pt)/K	$\log(a_{\mathrm{Pt}})$	$\log(J/\mathrm{m}^{-3}\mathrm{s}^{-1})$
800	0.07	1114	27.85	33.48
800	0.05	1058	27.70	33.15
800	0.035	1017	27.55	32.84
800	0.02	998	27.32	32.27
900	0.07	1280	24.17	33.60
900	0.05	1188	24.02	33.22
900	0.035	1085	23.87	32.71
900	0.02	1060	23.65	32.22
1000	0.07	1193	21.24	33.42
1000	0.05	1255	21.08	33.15
1000	0.035	1262	20.93	32.76
1000	0.02	1161	20.71	32.06

critical nucleus by using such correlation. This is unphysical and it appears that the nucleation theorem cannot be applied to such type of correlation function. Generally speaking, the activities in the mixtures should be lower than the pure substance activities for the same temperature and the same nucleation rate in order to obtain a positive number of atoms in the critical nucleus. Since this is not the case for the system investigated here we have omitted the analysis with the nucleation theorem using a correlation function. The reason for the shift of the activities in the binary system (marked by arrows in Figs. 7a and 7b) is the energy transfer from the nucleating Pt system to the Fe monomers as described above.

As an alternative we have also calculated the activities from the given constant carrier gas temperatures and the total number of atoms in the supersaturated vapour phase prior to nucleation. The resulting data are listed in Tables 2b, 2c and 2d for the binary data and for the pure Fe and pure Pt data. We have employed these activities for the analysis of pure Fe nucleation before [44] in order to compare to experimental data, which are usually based on the initial state conditions. This leads to the same activities for simulations at the same initial conditions. Therefore the effective nucleation rates obtained from three independent simulations at the same conditions are averaged and plotted in Figures 7c and 7d. In this plot the data exhibit a more systematic behaviour. In Figures 7e and 7f the same is done for only one carrier gas temperature (1000 K) but plotted using a non-logarithmic scale exemplarily. The view from the top of the three-dimensional diagram shown in Figure 7d looks also more systematic than Figure 7b. The activities of the binary systems are always at slightly lower values than the activities of the corresponding pure metal systems. This is however a small difference which is virtually invisible in the double logarithmic plot in Figure 7d. For a given carrier gas temperature the data of pure Fe, pure Pt, and the mixture rather form a right angle in the double logarithmic plot. Such data are also difficult to correlate by a plane which is not bent backwards such as the plane shown in Figure 7g is. Although the calculation of the activities from the initial conditions (carrier gas temperature and the initial number of metal monomers) yields a systematic behaviour of the nucleation rates, it also difficult to apply the binary nucleation theorem using a correlation function. As a source for this difficulty we consider the difference in the activities of the two substances by a factor of at least 10^7.

Since the application of the nucleation theorem is difficult for the investigated system the size of the critical nucleus has to be estimated in a different way. The size of the largest cluster in the system not losing any atoms has been used before [45] for testing the consistence to the critical nucleus size obtained from the correlation functions of

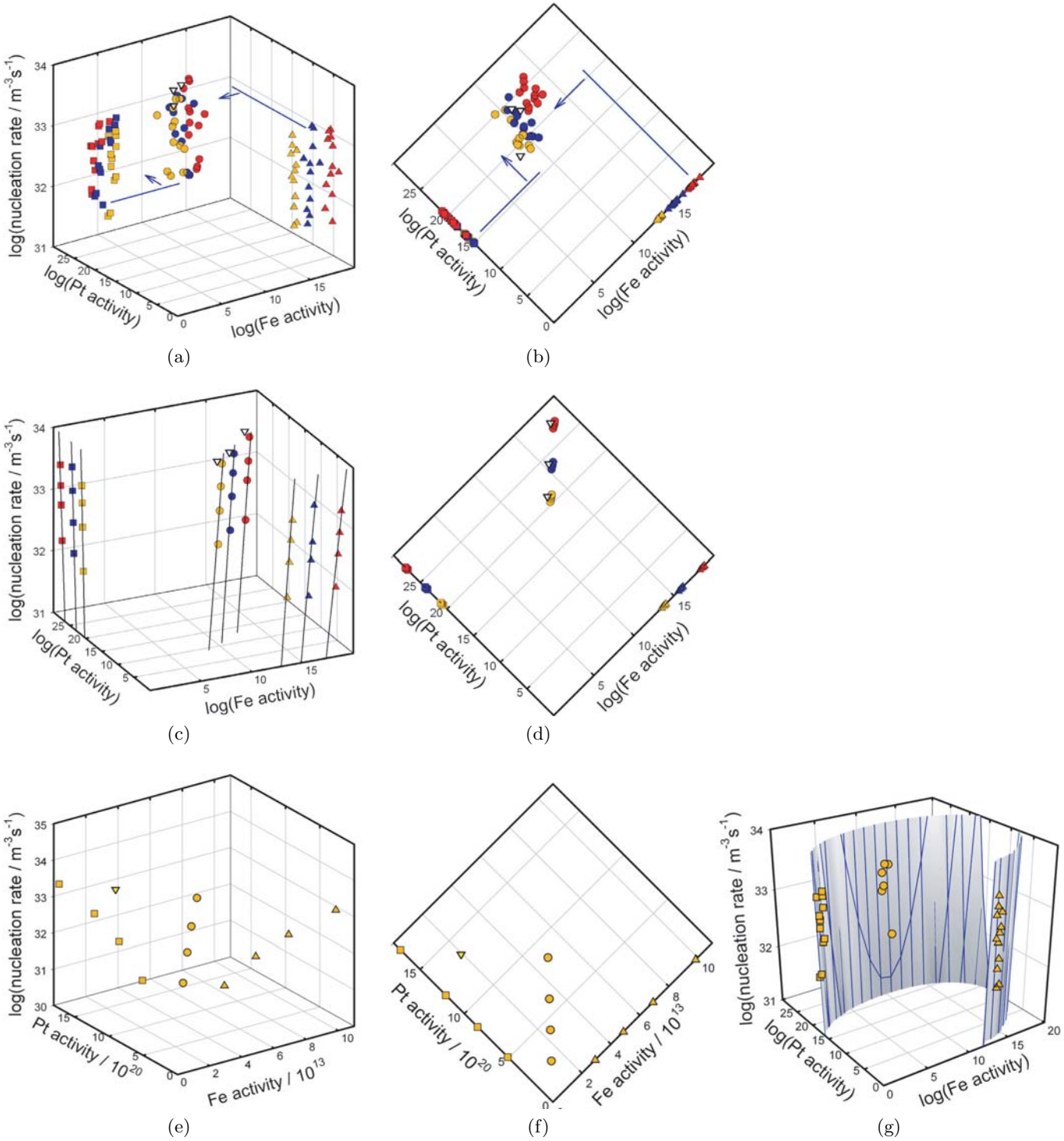

Fig. 7. (Color online) Nucleation data including the pure nucleation data for Fe [44] and Pt [45] and the binary nucleation data obtained here. (a) Activities calculated from the monomer number and temperature during nucleation for carrier gas temperatures 800 K (red/dark grey), 900 K (blue/black) and 1000 K (ochre/light grey). Triangle up: pure Fe; square: pure Pt; circles: $x_{\mathrm{Pt}} = 0.5$; open triangles down: $x_{\mathrm{Pt}} = 0.8$. (b) As (a) with view from top. (c) As (a) but with activities calculated from the carrier gas temperature and the total number of atoms of each metal in the simulation box. (d) As (c) with view from top. (e) As (a) but for $T(\mathrm{Ar}) = 1000$ K only and in non-logarithmic scale. (f) As (e) with view from top. (g) Nucleation rate data for $T(\mathrm{Ar}) = 1000$ K with activities calculated from the monomer number and monomer temperature during nucleation. The surface is a correlation function. The blue curves in the surface are sections at constant activity of either Fe or Pt.

pure Pt nucleation rates. It turned out that the number of atoms in the largest cluster not losing any atoms is always slightly larger than the critical nucleus size obtained from the correlation using the nucleation theorem. Here, for cluster sizes around 10 atoms the growth curve rises rapidly as one can see in Figure 5d for mixed clusters. The kink at the boundary between slow and rapid growth can be found at different times for different densities but at almost the same number of atoms in the largest cluster of 8 to 10. Beyond this cluster size a cluster can still lose atoms but these are rather evaporation events than density fluctuations taking place in the nucleation regime. In summary one can estimate the critical nucleus size to be around 5 to 10 atoms. The critical mole fraction can be estimated by taking a look at the cluster composition for cluster of this size around and below 10 atoms. The composition at this size is clearly $x_{\mathrm{Pt}} > 0.5$ as shown in Figure 4a. This suggests a critical nucleus mole fraction of about $x_{\mathrm{Pt}} = 2/3$.

5 Conclusion

The investigation of the binary nucleation and growth in the FePt system has shown some special features that can be related to the fact that the interactions between the Fe and the Pt atoms have different strength. Pt nucleates first because the attraction between Pt atoms is stronger than between Fe atoms. This leads to the formation of pure Pt clusters with up to 10 to 15 atoms. The heat of condensation for Pt is larger than for Fe. As a consequence in a small mixed cluster the Fe atoms will evaporate more likely because the temperature level of the cluster is dominated by the Pt atoms and therefore higher than for the formation of pure Fe clusters. One finds that the frequency of Fe evaporation is higher than in pure Fe systems. In addition larger clusters exhibit Fe evaporation because of this Pt-condensation heat effect. In a limited region at the beginning of the particle formation the Fe atoms rather act as a carrier gas for the Pt nucleation process. Due to the strong difference in attraction strength the effects found here are relatively large. In systems with less attraction and smaller differences in attraction, as in case of binary nucleation of molecular fluids, these effects are much smaller. Investigations by Mirabel and Katz [27] have shown that a very small amount of H_2SO_4 can lead to binary nucleation with water. This clearly shows the difference to the metal systems treated here.

This work has been supported by the Deutsche Forschungsgemeinschaft (DFG) within project Kr 1598/24-1.

References

1. R. Becker, W. Döring, Ann. Phys. **24**, 719 (1935)
2. M. Volmer, A.Z. Weber, Z. Phys. Chem. **119**, 277 (1926)
3. S.L. Girshick, C.P. Chiu, J. Chem. Phys. **93**, 1273 (1990)
4. H. Reiss, W.K. Kegel, J.L. Katz, J. Phys. Chem. **102**, 8548 (1998)
5. X.C. Zeng, D.W. Oxtoby, J. Chem. Phys. **94**, 4472 (1991)
6. V. Talanquer, D.W. Oxtoby, J. Chem. Phys. **100**, 5190 (1994)
7. P. Rein ten Wolde, D. Frenkel, J. Chem. Phys. **109**, 9901 (1998)
8. B. Chen, J.I. Siepmann, K.J. Oh, M.L. Klein, J. Chem. Phys. **116**, 4317 (2002)
9. R. Strey, Y. Viisanen, P.E. Wagner, J. Chem. Phys. **103**, 4333 (1995)
10. J. Hruby, Y. Viisanen, R. Strey, J. Chem. Phys. **104**, 5181 (1996)
11. J.Wölk, R. Strey, J. Phys. Chem. B **105**, 11683 (2001)
12. A. Fladerer, R. Strey, J. Chem. Phys. **124**, 164710 (2006)
13. R.G. Renninger, F.C. Hiller, R.C. Bone, J. Chem. Phys. **75**, 1584 (1981)
14. G. Wilemski, J. Chem. Phys. **80**, 1370 (1984)
15. G. Wilemski, J. Chem. Phys. **88**, 5134 (1988)
16. B.E. Wyslouzil, G. Wilemski, R. Strey, C.H. Heath, U. Dieregsweiler, Phys. Chem. Chem. Phys. **8**, 54 (2006)
17. H. Reiss, J. Chem. Phys. **18**, 840 (1950)
18. D. Stauffer, J. Aerosol. Sci. **7**, 319 (1976)
19. R. Strey, Y. Viisanen, J. Chem. Phys. **99**, 4693 (1993)
20. A. Laaksonen, M. Kumala, P.E. Wagner, in *Nucleation and Atmospheric Aerosols*, edited by N. Fukuta, P.E. Wagner (Deepak, Hampton, 1992)
21. D. Kashchiev, J. Chem. Phys. **76**, 5098 (1982)
22. Y. Viisanen, R. Strey, H. Reiss, J. Chem. Phys. **99**, 4680 (1993)
23. D.W. Oxtoby, D. Kashchiev, J. Chem. Phys. **100**, 7665 (1994)
24. P. Wagner, R. Strey, J. Phys. Chem. B **105**, 11656 (2001)
25. Y. Viisanen, P.E. Wagner, R. Strey, J. Chem. Phys. **108**, 4257 (1998)
26. P. Mirabel, J.L. Katz, J. Chem. Phys. **60**, 1138 (1974)
27. P. Mirabel, J.L. Katz, J. Chem. Phys. **67**, 1697 (1977)
28. Y. Viisanen, R. Strey, A. Laaksonen, M. Kulmala, J. Chem. Phys. **100**, 6062 (1994)
29. J.A. Nuth, K.A. Donnelly, B. Donn, L.U. Lilleleht, J. Chem. Phys. **85**, 1116 (1986)
30. M.M. Rudek, J.L. Katz, H. Uchtmann, J. Chem. Phys. **110**, 11505 (1999)
31. B. Giesen, A. Kowalik, P. Roth, Phase Transitions **77**, 115 (2004)
32. E. Goupil, P. Fouilloux, R. Maurel, React. Kinet. Catal. Lett. **35**, 185 (1987)
33. D. Weller, S. Sun, C. Murray, L. Folks, A. Moser, IEEE Trans. Mag. **37**, 2185 (2001)
34. T.J. Klemmer, N. Shukla, C. Liu, X.W. Wu, E.B. Svedberg, O. Mryasov, R.W. Chantrell, D. Weller, M. Tanase, D.E. Laughlin, Appl. Phys. Lett. **81**, 2220 (2002)
35. A. Moser, K. Takano, D.T. Margulies, M. Albrecht, Y. Sonobe, Y. Ikeda, S. Sun, E.E. Fullerton, J. Phys. D: Appl. Phys. **35**, R157 (2002)
36. B. Rellinghaus, S. Stappert, M. Acet, E.F. Wassermann, Proc. Mat. Res. Soc. **705**, 315 (2002)
37. H. Zeng, J. Li, Z.L. Wang, J. Ping Liu, S. Sun, IEEE Trans. Magn. **38**, 2598 (2002)
38. N.Lümmen, T. Kraska, Nanotechnology **15**, 525 (2004)
39. F.H. Stillinger, J. Chem. Phys. **38**, 1486 (1963)
40. H. Reiss, A. Tabazadeh, J. Talbot, J. Chem. Phys. **92**, 1266 (1990)
41. I.J. Ford, Phys. Rev. E **56**, 5615 (1997)

42. P. Rein ten Wolde, D. Frenkel, J. Chem. Phys. **109**, 9901 (1998)
43. D. Reguera, H. Reiss, Phys. Rev. Lett. **93**, 165701 (2004)
44. N. Lümmen, T. Kraska, J. Aerosol Sci. **36**, 1409 (2005)
45. N. Lümmen, T. Kraska, Nanotechnology **16**, 2877 (2005); note that parameter b of equation (2) has a positive sign, the negative sign is a misprint
46. P. Erhart, K. Albe, Appl. Surf. Sci. **226**, 12 (2004)
47. M.S. Daw, M.I. Baskes, Phys. Rev. Lett. **50**, 1285 (1983)
48. M.S. Daw, M.I. Baskes, Phys. Rev. B **29**, 6443 (1984)
49. S.M. Foiles, M.I. Baskes, M.S. Daw, Phys. Rev. B **33**, 7983 (1986)
50. E. Clementi, C. Roetti, At. Data Nucl. Data Tables **14**, 177 (1974)
51. A.D. McLean, R.S. McLean, At. Data Nucl. Data Tables **26**, 197 (1981)
52. R. Meyer, P. Entel, Phys. Rev. B **57**, 5140 (1998)
53. N.Lümmen, T. Kraska, Phys. Rev. B **71**, 205403 (2005)
54. N.Lümmen, T. Kraska, Comp. Mat. Sci. **35**, 210 (2006)
55. S.M. Foiles, Phys. Rev. B **32**, 3409 (1985)
56. J.F. Ziegler, J.P. Biersack, U. Littmark, *The Stopping and Range of Ions in Solids* (Pergamon Press, New York, 1985)
57. C.B. Alcock, V.P. Itkin, M.K. Horrigan, Can. Metall. Quart. **23**, 309 (1984)
58. K. Yasuoka, M. Matsumoto, J. Chem. Phys. **109**, 8451 (1998)
59. T. Kraska, J. Chem. Phys. **124**, 054507 (2006)
60. J.L. Rousset, A.M. Cadrot, F.J. Cadete Santos Aires, A. Renouprez, P. Mélinon, A. Perez, M. Pellarin, J.L. Vialle, M. Broyer, J. Chem. Phys. **102**, 8574 (1995)